https://doi.org/10.62836/iaet.v1i1.1004

Global Science Publishing

IAET

Innovations in Applied Engineering and Technology

https://ojs.sgsci.org/journals/iaet

Article

Optimization of Particle Distribution in Al-SiC Metal-Matrix Composite (MMC) Brake Rotors

Kang Heng

Department of Mechanical Engineering, The Ohio State University, Columbus, OH 43210, USA

Abstract: This paper presents a study of Al-SiC$_p$ metal matrix composite (MMC) brake rotors based on microscopic characterization, macroscopic thermomechanical tests and two-scale finite element analyses (FEA) aiming at rotor optimization. The objective is to achieve lower thermal stress of the rotor in working condition. The MMC microstructure and composition is confirmed under SEM, which also provides the micron-scale FEA geometry. Homogenized composite properties from micron-scale FEA is used to inform cm-scale FEA simulation of the realistic braking events. The simulated stress and temperature profiles in the brake rotor are compared against braking dyno tests to calibrate the FEA model, as well as quantifying the coefficient of friction (COF) evolution during the braking process. The dyno tests reveal that COF decreases with increasing sliding speed at temperatures ranging from 18 °C to approximately 350 °C. At a given sliding speed less than 50 mph, COF first increases and then decreases with increasing temperature, before reaching the brake fade limit of 350 °C. The FEA-based parametric study indicates that the peak macroscopic thermal stress in a braking event could be reduced by 31.8% with the optimized SiC distribution. The key to the minimization of in-brake thermal stress is found to be the accurate engineering of spatial distribution gradient of SiC particles in the transition Region linking the surface-under-friction and the hub Region around the bearing.

Keywords: Al-SiC metal-matrix composite (MMC); finite element analysis (FEA); automotive brake rotor optimization; multi-physics simulation; design of experiment (DoE); microstructural characterization

1. Introduction

Aluminum alloys are widely used in the automotive industry to achieve higher fuel economy due to their high specific mechanical properties [1]. Building on the existing popularity of Al alloys in the automotive industry, aluminum metal-matrix composites (MMCs) have been developed for the purpose of enhancing its specific thermo-mechanical properties, especially under intensive working conditions such as those experienced by brake rotors. In this class of MMCs, those with silicon carbide (SiC) reinforcement particles present a good combination of cost, properties and compatibility with other automotive components. In addition to improvement of the mechanical and thermal performances, Al-SiC can be "tuned" to achieve macroscopic isotropy in key properties through optimizing particle distribution, making them a good substitute material for high-end brakes such as those used in racecars and airplane landing gears [2].

In traditional cast iron disc brakes, severe and repeated non-homogeneous friction-induced cyclic thermo-mechanical loading is a primary cause of fatigue cracks in brake discs, and this concern applies equally in the

Received: 15 October 2022; Accepted:18 November 2022.

Corresponding: Heng Kang (kang.641@osu.edu)

design and manufacturing of MMC brakes as well [3]. To address this problem, extensive studies on the braking process have been conducted. Developed an analytical model for the heat transfer in a brake system [4]. 2D axisymmetric and 3D finite element analysis (FEA) model were developed by to analyze heat transfer of a disc brake [5 – 7]. In the 3D models, non-axisymmetric load and the temperature dependent coefficient of friction between brake disc and brake pad were taken into account. However, none of the above numerical studies established connection between the FEA models and practical experiment.

COF between the brake rotor and brake pads is critical in determining the braking power and heat generation. Shorowordi investigated the influence of velocity on COF between aluminum MMCs reinforced with SiC and B4C particles and commercial phenolic brake material with pin-on-disc experiment [8]. They found that higher sliding velocity leads to lower friction coefficient for both MMCs. Studied the influences of sliding speed and load on the COF between A359-20 vol.% SiC particle composite and automobile friction material through pin-on-disc experiments [9]. They concluded that the sliding speed did not have significant effect on COF at applied load range between 50 N to 100 N. Muratoglu explored the influence of sliding surface temperature on COF between 25 vol.% SiC reinforced 2124 aluminum alloy composite and AISI 1050 steel with pin-on-disc experiment [10]. They found that COF between MMC and steel decreased at first as the temperature increased from room temperature to around 80 °C and after that COF increased as the temperature increased. The friction between Al-SiC MMC brake rotor and automobile friction material is a complex process and the COF is determined by load, sliding speed and temperature. The above researchers studied the influence of the three factors. However, the influence of load and sliding speed always coupled with the influence of temperature. Little information is available in the literature on the decoupled influence of the three factors on COF, which is important for an accurate numerical study on the braking process and constitutes an important part of the present study

The objective of this work is the optimization of the SiC distribution in the brake rotor through experimentally-informed FEA at the particle scale (tens of μm) and the disc scale (tens of cm). Starting from understanding the material's microstructure and composition, Section 2 documents the scanning electron microscope (SEM) and energy dispersive spectroscopy (EDS) analyses. Based on the SEM micrographs, properties of the MMC with different particle contents are computed by particle-scale 2D FEA. Section 3 presents the macroscopic scale thermo-mechanical testing in which pad-rotor coefficient of friction (COF) and rotor temperature evolution are measured in temporally consecutive dyno tests. Section 4 presents the FEA model incorporating the experimentally-measured COF and calibrated to the dyno tests, and aims at recovering the instantaneous temperature on the sliding surface and decoupling the dependences of COF on sliding speed and on the surface temperature. Section 5 presents the parametric study to explore different SiC distribution profiles for reduced in-service thermal stress in the brake rotor. Section 6 summarizes the findings and physical insights obtained in this work.

2. Microstructural Characterization

To confirm the composition and microstructure of the as-received material, SEM and EDS analyses are conducted to study the morphology of the composite in micrometer scale and to confirm the chemical constituents, respectively.

2.1. Scanning Electron Microscopy

Microstructural characterization is conducted with Quanta 200 scanning electron microscope. Figure 1 shows the SEM images of the composite under different magnifications. Micrographs from the Everhart-Thornley detector (ETD), which mainly reflect surface morphology, and from the Solid State detector (SSD), which mainly reflect the chemical composition, are contrasted in Figure 1a,b for the same Regions.

Three different phases are identified in Figure 1, as labelled in the SSD image in Figure 2. The matrix phase, labelled by 1 in Figure 2, occupies the largest percentage of each micrograph. The embedded phases include a darker and elongated type, labelled by number 2, and a brighter-than-matrix type, labelled by number 3. The composition of these phases is determined by energy dispersive spectroscopy as presented below.

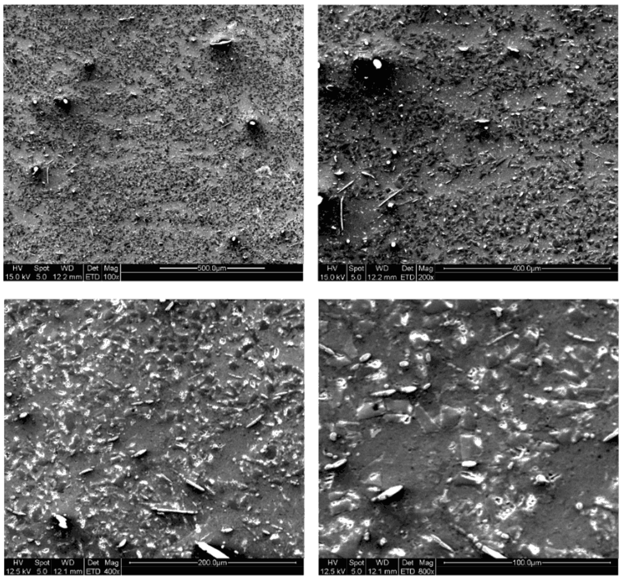

(a) Surface morphologies (through ETD)

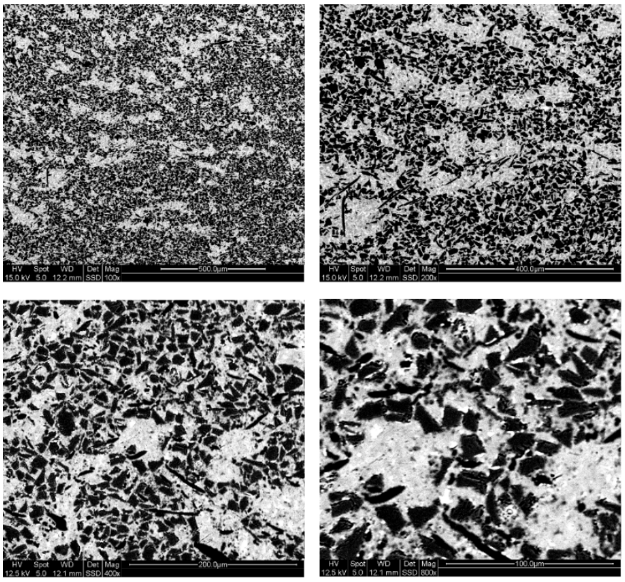

(b) Surface elemental mapping (through SSD)

Figure 1. SEM images of the composite through (**a**) Everhart-Thornley detector, and (**b**) Solid State detector.

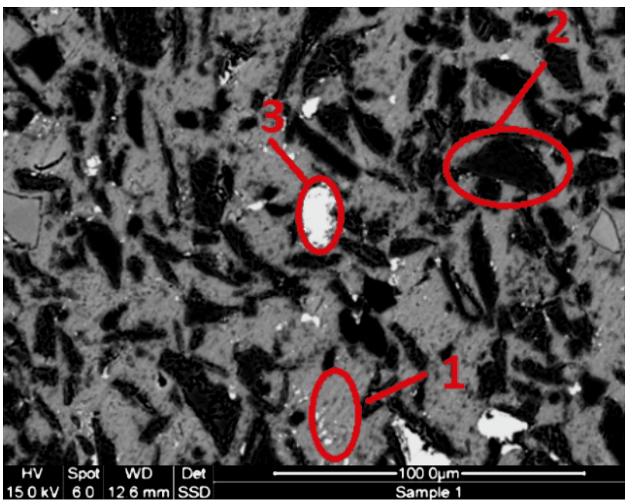

Figure 2. Three featured Regions in SEM solid-state detector image.

2.2. Energy Dispersive Spectroscopy

In order to determine the chemical composition of each type of microstructure, EDS analysis is conducted on Quanta 200. By keeping the electron beam focused on spots inside each of the three Regions, the EDS analysis provides localized elemental information by recording their characteristic X-ray photon energies and intensities. Tables 1–3 show the elemental composition of the three Regions respectively.

As summarized in Table 1, Al accounts for 98.10 at.% of the matrix, which is consistent with the expectation that the matrix constitutes mainly of aluminum. Quantitatively, however, the measured aluminum content is higher than the nominal Al content of ~93 at.% in commercial A319 alloy [11]. The reason for this discrepancy will be evident below. Table 2 shows that the darker elongated Regions are indeed SiC reinforcement particles as expected. Finally, the bright spots typified by Region 3 in Figure 2 turn out to be a distinct phase unaccounted by the manufacturer. Table 3 shows that it is rich in heavier substitutional elements such as Fe (32.88 wt.%), Cu (1.81 wt.%) and Ti (2.04 wt.%). Moreover, this phase is typically observed on the surfaces of SiC particles, as evident by the increase of measured contents of Si and C elements when the acceleration voltage increases. These observations strongly suggest that precipitation of substitutional elements occurred during the fabrication of the MMC rotors, and the matrix particle interface provides favorable sites for such precipitation. As a result, the matrix composition is altered after the fabrication of MMC, being depleted of heavier substitutional elements.

Table 1. Chemical composition of Figure 2 Region 1, identified as the matrix.

Element	Weight %	Atomic %
Al	98.02 ± 1.73	98.10 ± 1.73
Si	1.98 ± 0.53	1.90 ± 0.51

Table 2. Chemical composition of Figure 2 Region 2, identified as a SiC reinforcement particle.

Element	Weight %	Atomic %
C	30.33 ± 6.04	50.45 ± 10.05
Si	69.67 ± 1.47	49.55 ± 1.05

Table 3. Chemical composition of Figure 2 Region 3, identified as a precipitate phase.

Element	Weight %	Atomic %
C	0.77 ± 0.35	2.12 ± 0.95
Cu	1.81 ± 0.27	0.94 ± 0.14
Al	46.78 ± 2.18	57.46 ± 2.68
Si	15.72 ± 1.06	18.55 ± 1.25
Ti	2.04 ± 0.33	1.41 ± 0.23
Fe	32.88 ± 1.31	19.51 ± 0.78

3. Dyno Tests

As mentioned in the introduction, pad-rotor COF varies with surface temperature and sliding speed in a complex manner. To establish the accurate dynamic COF for our rotor system, speed-controlled braking tests, otherwise known as dyno tests, are conducted in which the dynamic frictional force is measured and converted into the COF history throughout the tests. In addition, rotor temperatures are monitored at two locations by pre-embedded thermocouples. These tests provide the benchmark of calibration as well as model input for subsequent FEA optimization effort. These tests are undertaken by manufacturer of the MMC rotor (REL, Inc., Calumet, MI, USA).

The sample rotor used in the dyno tests has a measured SiC volume fraction of approximately 40%

throughout the disc Region (excluding the hat and fin structure, which are pure A319). The brake pad material is RF 50 from Scan-Pac Manufacturing, and it is a rigid molded phenolic friction material. Figure 3 shows the experiment setup for the dyno tests.

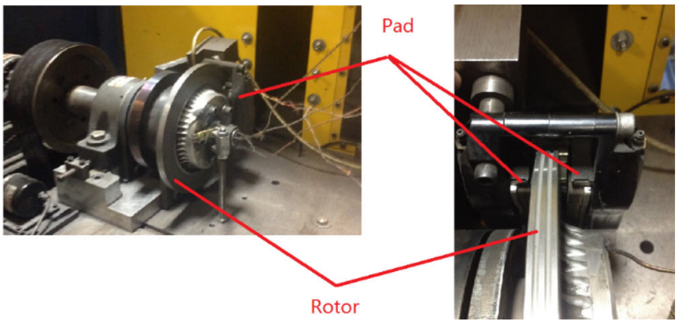

Figure 3. Experiment setup of the dyno tests.

Two thermocouples were embedded in the rotor at locations shown in Figure 4 along with their measured temperature history. As shown in Figure 5a, the tests consist of five consecutive braking events (stops). In each stop, the rotational speed is reduced from the peak value of 68.2 rad/s to 0 rad/s. The total standby and reacceleration time between neighboring events is approximately 22.5 s. This protocol is to ensure the coverage of a sufficiently large surface temperature range. The first stop starts at room temperature. The pad pressure is maintained at 2 MPa during each stop. The measured COF history is shown in Figure 5b.

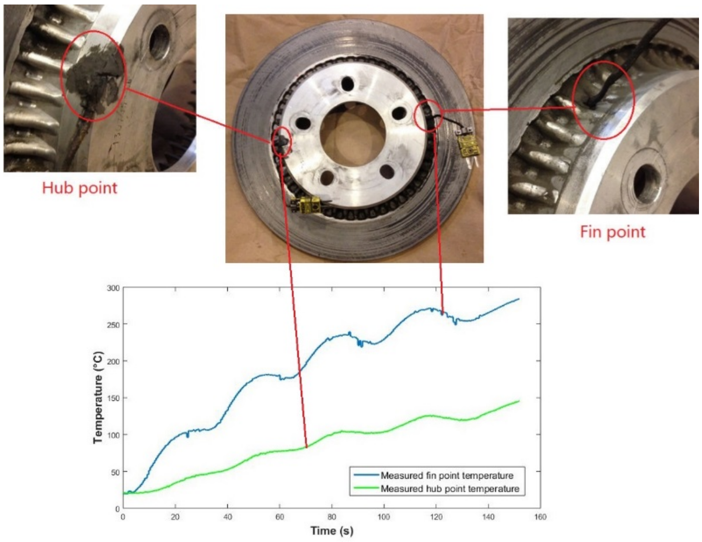

Figure 4. Locations of the thermocouples, hub point: halfway down side of the aluminum hub, fin point: between cooling fins, pressed against hubs outer surface.

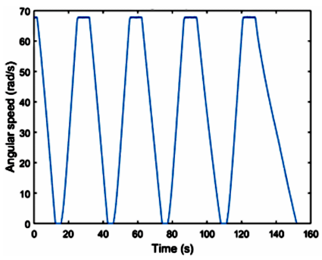

(a) Rotational angular speed history

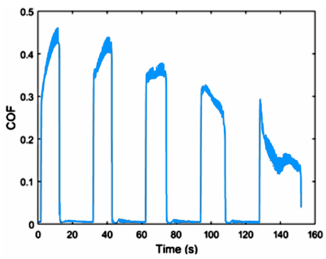

(b) Measured COF history

Figure 5. Measured rotational speed and COF history from the dyno tests.

The instantaneous COF and angular speed are shown in Figure 5. The oscillation of COF may have resulted from the run-out of the rotating disc, as previously reported [12]. The average COF for each stop decreases dramatically from the third stop onward, as shown in Figure 5b, when the measured temperature at the fin point exceeds 200 °C, as shown by the blue curve in Figure 4. The COF decrease is believed to be a result of increasing sliding surface temperature, which is even higher than the measured value by the fin point thermocouple. In order to accurately account for the COF variation, we now proceed to simulate the dyno tests in 3D FEA with the aim of back-inferring the sliding surface temperature by reproducing the measured temperature profiles at hub point and fin point.

4. Finite Element Model Setup and Calibration

In order to optimize the reinforcement distribution in the rotor, 3D FEA accounting for all major thermal stress mechanisms is developed and calibrated in this section. This cm-scale rotor model, which incorporates the homogenized composite properties as well as joule heat generation, conduction, convection and radiation, is calibrated against the dyno tests presented in the previous section. The measured COF and angular speed data are incorporated from the tests, and the effect of friction is simplified as distributed heat sources on the rotor sliding surfaces. All other testing conditions are in agreement with actual testing protocol. The model is calibrated against the temperatures data measured by the preinstalled thermal couples (Figure 4).

4.1. Physical Framework

Essentially, the FEA solves the differential heat transfer equation on every material point of the rotor. The equation is given by

Heat generation and heat transfer mechanisms–namely, conduction, convection and radiation–are considered in the model, as presented separately below.

$$\rho C\frac{\partial T}{\partial t}+\rho C\vec{u}\cdot\nabla T=\nabla\cdot(k\nabla T)+Q \tag{1}$$

where ρ is density, C is specific heat capacity (J/(kg·K)), $\vec{u}$ is the velocity vector of each point, k is thermal conductivity (W/(m·K)), Q is the total heat influx rate into the rotor, which is the sum of the conduction, convection and radiation influx rates:

$$Q=\xi\phi(r,t)-\varepsilon\sigma(T^4-T_{ambient}^4)-h(T-T_{ambient}) \tag{2}$$

The generated heat flux density $\phi(r,t)$ is given by:

$$\phi(r,t)=\frac{p(t)\mu(t)\omega(t)rdA}{dA}=p(t)\mu(t)\omega(t)r \tag{3}$$

where r is the distance to the center of the rotor, $p(t)=2$ MPa is the pressure maintained between the rotor and the pads, $\omega(t)$ is the angular speed, $\mu(t)$ is the COF between the rotor and the pads. The plot of $\omega(t)$ and $\mu(t)$ are given in Figure 5.

The heat partition coefficient ξ is given by [4]:

$$\xi=\frac{\sqrt{k_{rotor}\rho_{rotor}C}_{rotor}\cdot S_{rotor}}{\sqrt{k_{rotor}\rho_{rotor}C}_{rotor}\cdot S_{rotor}+\sqrt{k_{pad}\rho_{pad}C}_{pad}\cdot S_{pad}} \tag{4}$$

with subscripts specifying the part, S is frictional contact surface. $T_{ambient}$ is the ambient temperature, ε is material emissivity and $\sigma=5.67\cdot10^{-8}$ (W/(m^2·K)) is Stefan-Boltzmann constant.

The convective coefficient is a function of rotational speed [13]:

$$h=\frac{0.027k}{D_{out}}\left(\frac{\rho D_{out}\omega r}{\mu}\right)^{0.8}\left(\frac{C\mu}{k}\right)^{0.33} \tag{5}$$

where D_{out} is the rotor outer diameter and μ is the viscosity of air at room temperature.

4.2. FEA Model

The 3D thermomechanical FEA model is developed with COMSOL Multiphysics [14]. The geometry of the brake rotor assembly is shown in Figure 6.

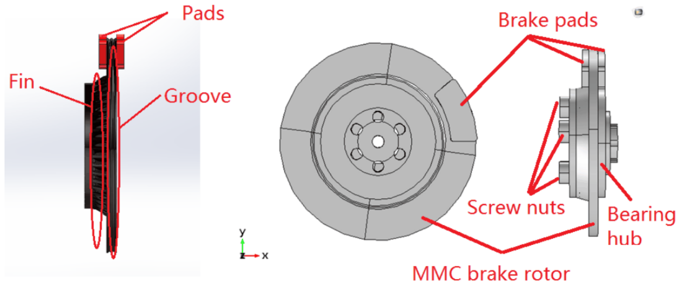

Figure 6. Geometry of the brake rotor assembly in the FEA model.

For computational simplicity purpose, the groove structure on the outer edge of the disc Region and fin structures are not modeled. The MMC brake rotor has SiC volume fraction of 40%. The brake pads material is RF 50 manufactured in Scan-Pac Manufacturing Inc. The screw nuts and bearing hub are stainless steel. The material properties of each phase in the brake rotor, (Al A319 and SiC), are provided from REL Inc. [15]. The properties of MMC with different SiC volume fraction are calculated with 2D SEM image based FEA models (Appendix A) as shown in Figure 7 (the data are normalized by setting the properties of Al A319 to be unit value). The properties of the brake pad material, RF 50, are provided by Scan-Pac Manufacturing. The assembly is meshed using tetrahedral elements with maximum element size of 8 mm and minimum element size of 1 mm depending on the location of the elements on the parts (Figure 8). The brake rotor, the bolts and the bearing hub is set to be static and the brake pads rotate to the center of the rotor with the angular speed measured in the experiment.

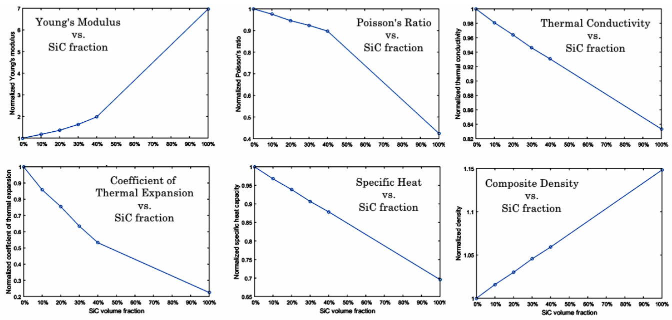

Figure 7. Normalized material properties of Al A319-SiC with different SiC volume fractions.

The measured COF between the brake rotor and the pads in the dyno tests is incorporated in the finite element model. The bearing hub is assumed to have heat transfer with the brake rotor only. The ambient temperature is set to be 18 °C under which the dyno tests are conducted. The material properties are assumed to be independent on the temperature and the pressure is assumed to be uniform over the contacting surface. The COF is assumed to be independent on the SiC volume fraction.

The temperatures of the fin point and the hub point (see Figure 9) are probed and compared with the

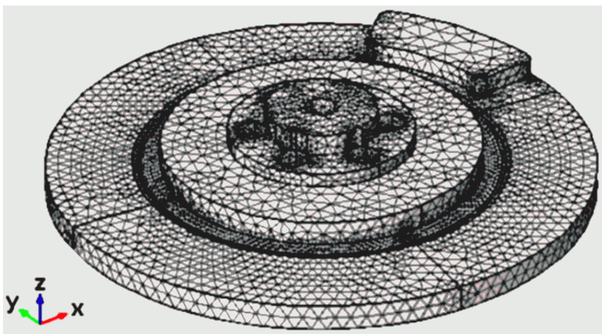

Figure 8. Mesh of the brake rotor assembly.

measured temperatures at respective points in the experiment. The calculated and measured temperatures, as shown in Figure 10, have the same trend and the differences between them are within reasonable range. For the fin point temperature, the calculated value has a higher rate of increase, which is probably due to the response time of the thermocouples in the experiment.

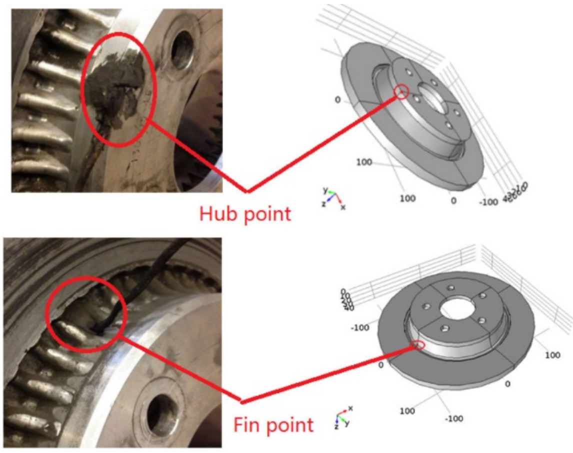

Figure 9. The corresponding locations of the thermocouples in the FEA model.

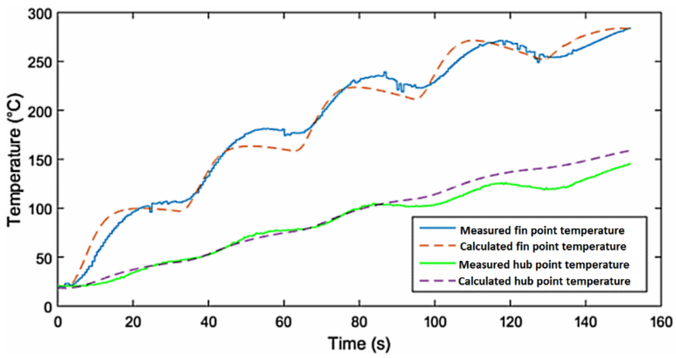

Figure 10. Comparison of the measured and calculated temperatures at fin point and hub point.

In order to investigate the influence of the sliding surface temperature on COF, the average temperature over the contact area between the brake rotor and the brake pads are calculated as the sliding surface temperature, the result of which is shown in Figure 11. Unlike the temperatures at the fin point and the hub point where the temperatures are increasing during the whole five stops, the sliding surface temperature has obvious decrease between each two stop events. That is because in the period between two stop events, there is no heat dissipated into the sliding surface on the rotor, but there is still heat conducted into the hub Region of the rotor and heat entered into air through convection and radiation. In addition, the sliding surface temperature is much higher than the _n point temperature which results in the brake fade at the end of fourth stop and the fifth stop.

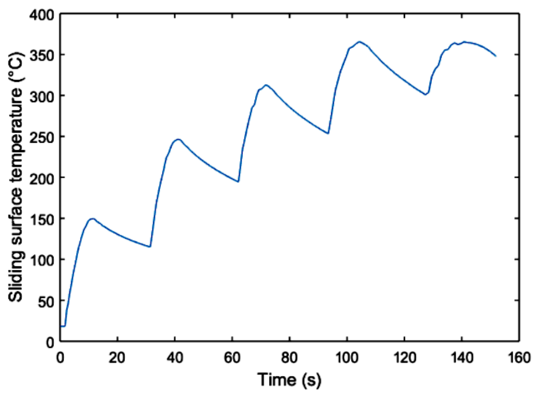

Figure 11. Sliding surface temperature from FEA simulation replicating the dyno tests.

4.3. COF Study

Given the measured data of vehicle speed and COF, and the calculated sliding surface temperature, the scatter plot of COF μ vs. sliding surface temperature T and vehicle velocity v is shown in Figure 12. An analytical 3D function of the form given in Equation (6) is used to fit the experimental COF data

$$\mu(v,T) = c_0 + c_1 v + c_2 T + c_3 vT + c_4 T^2 + c_5 (T-300)^2 \operatorname{sgn}(T-300) \quad (6)$$

where c_0 through c_5 are fitting coefficients whose determined values and 0.95 confidence range is given in Appendix B. From Equation (6), the dependence of COF between the Al A319/SiC brake rotor and RF 50 brake pad under 2 MPa pressure on sliding surface temperature with different sliding speed is shown in Figure 13.

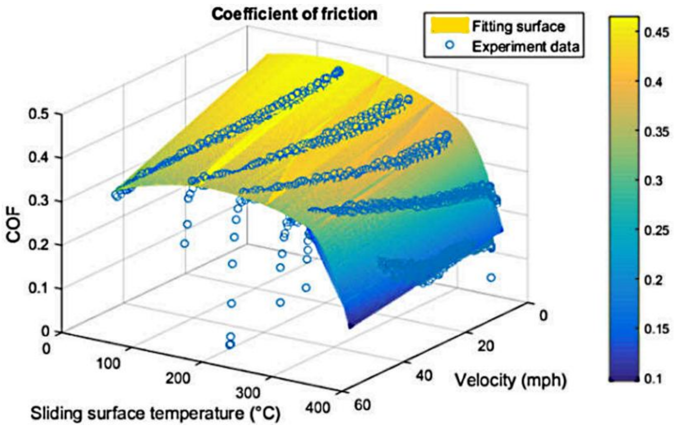

Figure 12. Impact of sliding surface temperature and velocity on COF at 2 MPa contact pressure.

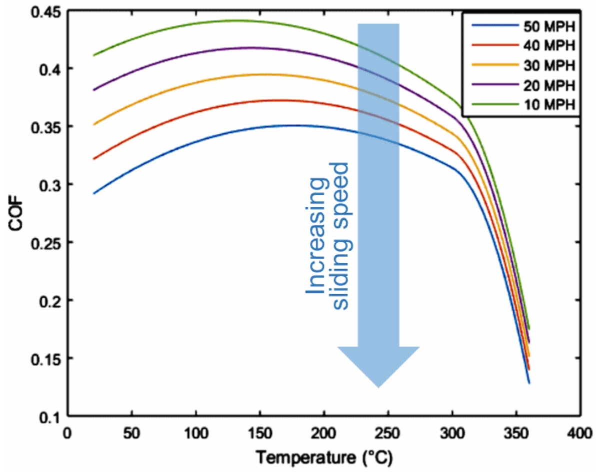

Figure 13. The COF dependence on sliding surface temperature between Al A319/ SiC brake rotor and RF 50 brake pad under 2 MPa pressure with different sliding speed.

At a given temperature, COF is higher at lower sliding speeds, which coincides with results in research on the COF between MMC brake rotor and phenolic brake pad [8]. At a given sliding speed, COF first increases from room temperature and then decreases. The mechanism of friction between the Al A319/ SiC brake rotor and RF 50 (non-asbestos, non-metallic) brake pad was adherent friction which documented in [16]. Adherent friction is one of the two types of friction mechanisms in brake and the other one is abrasive friction where abrasive particles in the pad are harder than the rotor material in crystalline sense. In the adherent friction, a thin transfer layer of brake pad material adheres to the brae rotor surface. The kinetic energy is then transferred to thermal energy through breaking the intermolecular bonds of the brake pad material, which is formed instantaneously before being broken. At a given temperature, fewer inter-molecular bonds are formed with higher sliding speed thus lead to lower friction coefficient. At a given speed, when the sliding temperature is increased from room temperature, the formation of the inter-molecular bonds is promoted, the transfer layer becomes “sticky”, and the COF increase with temperature. However, when the temperature increases to above

150 °C, the transfer layer loses its adhesiveness onto the rotor surface gradually which leads to the reduction of COF. At temperatures higher than about 350 °C, the transfer layer becomes "slippery", the brake power is lost and brake fade happens.

5. Optimization of SiC Distribution in the Brake Rotor

5.1. Parametric Study

As evident in Figure 7, the thermal and mechanical properties of the MMC depend on the SiC volume fraction. Thus, lower thermal stress can be achieved by optimizing the SiC distribution inside the rotor, reducing the amplitude of cyclic thermal load from braking which contributes to rotor fatigue failure.

Of the three cylindrical coordinate directions, namely r, ϕ and z, major thermal mismatch stress component exists in the r direction. Therefore, the parametric study in this paper focuses on the RVF distribution along the radius direction in the brake rotor. The distribution design space is parametrized into SiC volume fractions at five strategic positions as shown in Figure 14, defining a radially piecewise linear profile throughout the rotor. The optimized SiC distribution can then be obtained by traversing the 5-parameter space in FEA and searching for the combination that minimizes the peak macroscopic thermal stress during a typical brake event (defined below).

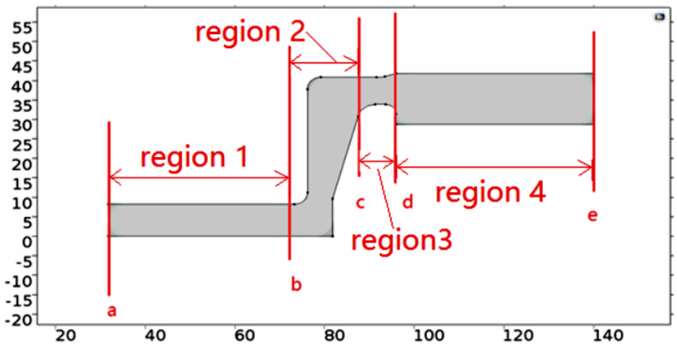

Figure 14. Cross-section of the brake rotor and parameters determining the piecewise linear SiC distribution in the radial direction. Of the five SiC volume fraction parameters, b, c and d correspond to edges of the three rounded chamfers.

As shown in Figure 14, SiC distribution profile is described by the the parameters a, b, c, d and e, each ranging from 0% to 40%—the upper limit being suggested by the rotor manufacturer in consideration of cost and manufacturing state-of-the-art. The SiC volume fraction varies linearly with radius in each Region.

The typical brake event used in the parametric study is defined as stopping a vehicle with a total mass of $m_{car} = 5000$ kgtraveling initially at $v(0) = 50$ mph in 10 s. Both upper and lower pads have a contact area of 5316 mm^2. The braking pressure is assumed to be 2 MPa throughout the event.

To save computational resources, pad-rotor contacts during the braking event is modeled as rotating heat sources with intensities corresponding to the power density of frictional Joule heat generation. The derivative of the vehicle kinetic energy equals to the integration of the heat flux density over the pad area S:

$$2\iint_S p(t)\mu(T,v)\omega(t)r \cdot dA = \frac{d(\frac{1}{8}m_{car}v_{car}^2)}{dt} \tag{7}$$

which leads to

$$a(t) = \frac{8p(t)\mu(T,v)\iint_S rdA}{mr_{wheel}} \tag{8}$$

The velocity of the vehicle is:

$$v(t) = v_0 - \int a(\tau)d\tau \tag{9}$$

where $a(\tau)$ is the deceleration of the vehicle at $t = \tau$. The angular speed of the brake pads is given by:

$$\omega(t)=\frac{v(t)}{r_{wheel}} \tag{10}$$

The angular speed obtained from Equation (10) is applied in the 3D FEA model. The COF is incorporated into the models from Equation (6).

It is found in 3D FEA that the maximum thermal stress always occur in Regions 2 or 3 in Figure 14. To reduce the investigated parameter space, the SiC volume fractions on the inner and outer edges, i.e., parameters *a* and *e*, are fixed *a priori*. The parameter *e* is maintained constant at 40% to ensure minimal high temperature creep, while parameter *a* is set as the same as *b*. It is confirmed throughout the course of this work that this simplification has no obvious impact on the resulting thermal stress field.

The parametric study is conducted in 2D axisymmetric FEA model whose geometry is shown in Figure 14. Friction heat sources applied in 3D FEA is reduced to time varying line heat sources on the top and bottom surfaces of Region 4. In other words, variation in the cylindrical ϕ direction is smeared out. The validity of 2D FEA is tested and confirmed by comparing its maximum von Mises stress vs. time curve with that from the corresponding 3D FEA. The peak stress prediction difference from the two models is found to be less than 6%.

In the 2D axisymmetric FEA model, the friction heat flux density is calculated through dividing the 3D heat flux density by the ratio of the brake pad area to the sliding area of brake rotor. Running the models with different combinations of *b*, *c* and *d*, the maximum von Mises stress under each combination of parameter is obtained.

5.2. Optimization Result

The parametric study result is shown in Figure 15 in terms of maximum von Mises stress through the whole braking process. It can be seen from the surface plot that the maximum von Mises stress depends sensitively on the SiC distribution in the transition regions between the rotor hat and rotor disk under friction. The maximum von Mises stress, which is always found in Region 3 regardless of parameter combinations, ranges from 80.1 MPa to 147.1 MPa with different SiC distributions. In other words, SiC distribution in the narrowest part (Region 3) determines the maximum thermal stress [17].

In general, the maximum thermal stress increases with increasing *b* and *c*. However, the dependence on *d* is non-monotonic when both *b* and *c* are close to 0. The peak stress is found to be minimized at $a = b = c = 0$, $d = 30\%$. This optimized SiC distribution profile is shown in Figure 16a, along with the temperature and temperature gradient contour in Figure 16b and Figure 16c, respectively.

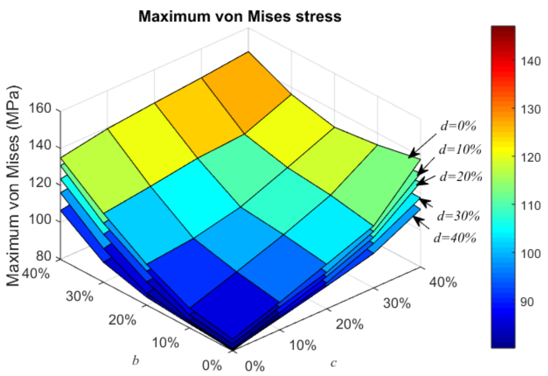

Figure 15. Maximum von Mises stress with different parameter combinations.

5.3. Discussion

Since the outer edge of the brake rotor has the highest sliding speed, thus the highest heat flux density into the outer edge, highest flash temperature is supposed to occur at the outer edge. Figure 17 shows the stress profile of the current and optimized brake rotor with 3D FEA model and their peak von Mises stress is 117.0 MPa at 8 s and 79.8 MPa at 7 s respectively. With both SiC distribution, the peak von Mises stresses occur at the fin region (Region 3 in Figure 14).

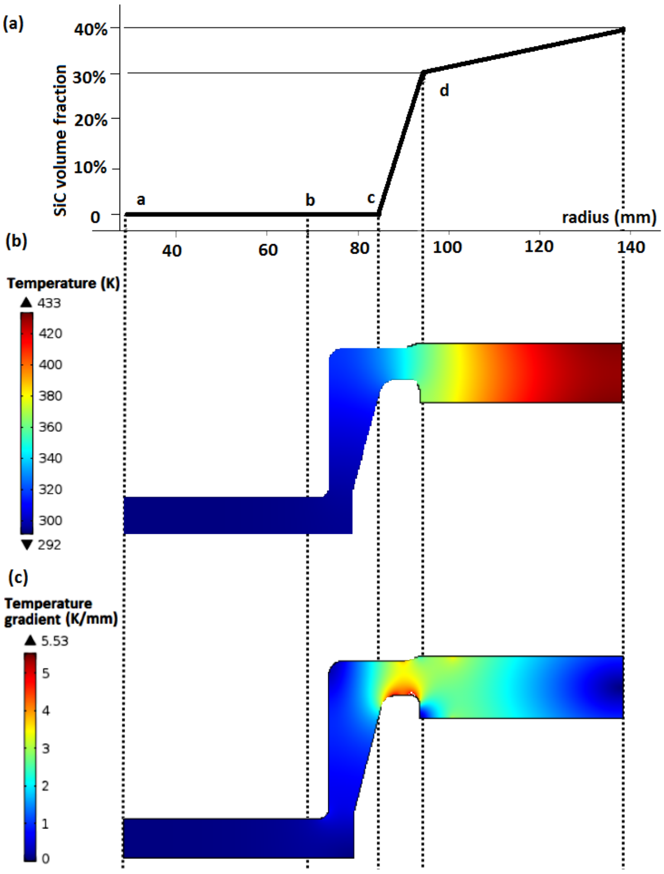

Figure 16. (**a**) Optimized SiC distribution, (**b**) temperature profile at t = 7 s, (**c**) temperature gradient profile at t = 7 s.

The comparison of maximum von Mises stress between current rotor and optimized rotor is shown in Table 4. The thermal stress within the brake rotor could be reduced 31.8% by adopting the optimized SiC distribution under the brake event in this paper.

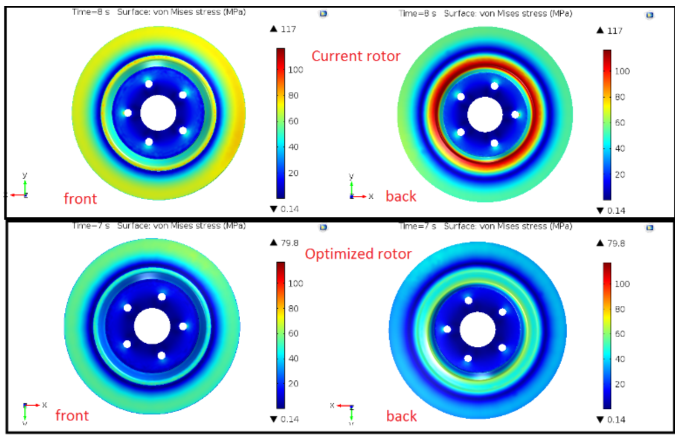

Figure 17. Maximum von Mises stress of current brake rotor at t = 8 s and optimized brake rotor at t = 7 s.

Figure 16a shows the optimized SiC distribution along the radius in the brake rotor. From Figure 16b, the temperature in Region 4 is much higher than that in Region 2 which leads to the high temperature gradient along the radius in Region 3 (Figure 16c). With the knowledge that the CTE of MMC has inverse relationship with SiC volume fraction, the Region with high temperature should have lower CTE thus higher SiC volume fraction. By that way, the thermal stress could be reduced by placing an inverse SiC volume fraction gradient to the temperature gradient in Region 3 to reduce the thermal expansion mismatch.

Table 4. Comparison between the current SiC distribution design and the optimized design.

	Current Rotor	**Optimized Rotor**	**Percentage**
Max. von Mise stress (MPa)	117	79.8	−31.8%
Combination of parameters	$a = b = c = d = 40\%$	$a = b = c = 0$, $d = 30\%$	

6. Summary/Conclusions

This paper investigates the influence of sliding speed and sliding surface temperature on COF between Al A319-SiC brake rotor and RF 50 brake pads quantitatively based on the experiment data in a series of braking dyno tests. At a given temperature, COF is higher at lower sliding speeds. At a given sliding speed, COF first increases from room temperature and then decreases. At temperature higher than about 350 °C, brake fade happens.

3D thermomechanical FEA model is developed incorporating the experiment data from the dyno tests and the FEA model is calibrated with the measured temperature data. Excessive thermal stress in the MMC brake rotor could lead to thermal fatigue cracks on the friction surface. Parametric study on the SiC distribution in the brake rotor is conducted in order to reduce the thermal stress in the brake rotor under working condition. The stress in the brake rotor would be reduced by 31.8% (in this paper's braking scenario) by adopting the optimized SiC distribution where an increase of SiC volume fraction is applied at the highest temperature gradient fin Region. In the future, experiments are to be conducted to characterize temperature dependent MMC properties and the results would be included in the FEA models.

Funding

This research was funded by the member organizations of the Smart Vehicle Concepts Center, a National Science Foundation Industry/University Cooperative Research Center (www.SmartVehicleCenter.org).

Institutional Review Board Statement

Not applicable.

Informed Consent Statement

Not applicable.

Data Availability Statement

Not applicable.

Conflicts of Interest

The author declares no conflict of interest.

Appendix A. MMC Properties Calculation with SEM Image Based 2D FEA

The SEM images of MMC with different SiC volume fraction are imported into the 2D FEA model. Virtual experiments on representative elements based on SEM images are conducted with COMSOL Multiphysics.

Appendix A.1. Calculation of Young's Modulus and Poisson's Ratio

Virtual tensile tests are conducted on the representative elements to obtain the effective Young's modulus and effective Poisson's ratio. The left and bottom edges of the representative element are set to be symmetric and a small displacement is assigned to the top surface (Figure A1). The Young's modulus is obtain by using the domain average longitudinal direction stress divided by the longitudinal strain, and the Poisson's ratio is obtained by using the negative value of the average transverse strain divided by the longitudinal strain. It is worth noticing that stress concentration exists and that the highest stress could be several times higher than the average value.

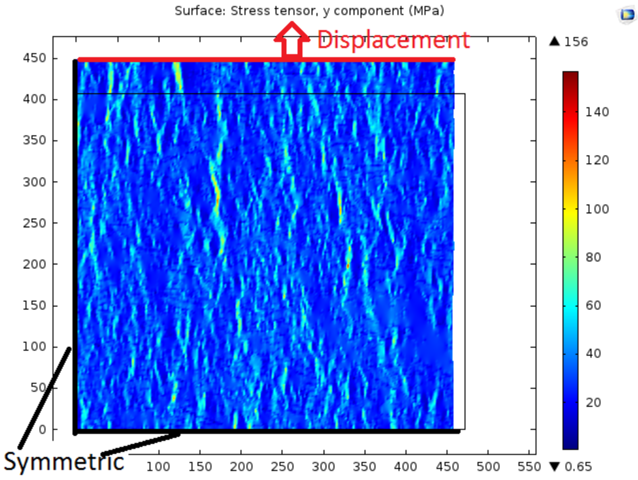

Figure A1. Boundary conditions and load of virtual tensile test and the longitudinal direction stress distribution.

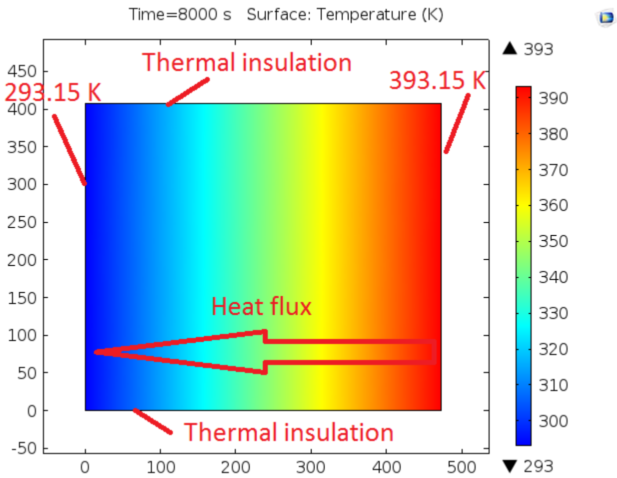

Figure A2. Boundary conditions of virtual heat conduction test and the temperature distribution at steady state.

Appendix A.2. Calculation of Thermal Conductivity

Virtual heat conduction tests are conducted to obtain the effective thermal conductivity. The top and bottom edges of the representative element are thermally insulated and the left and right edges are set to be 291.15 K and 393.15 K (Figure A2). The instantaneous heat flux density on the right edge is recorded when the heat conduction process comes into steady state, the heat flux density becomes a steady value. The effective thermal conductivity K could be obtained from the formula:

$$K = \frac{Q \cdot \Delta x}{\Delta T} \tag{A1}$$

Q is heat flux, Δx is the dimension of the edge perpendicular to the heat transfer direction and ΔT is the temperature difference between the left and right edges.

Appendix A.3. Calculation of Coefficient of Thermal Expansion

Virtual heating tests are conducted to the representative element to calculate CTE of MMCs. The mechanical boundary condition for this test is the same as the virtual tensile test and the representative element is heated by a domain heat source. The CTE of the MMC α_c could be obtained from the formula:

$$\alpha_c = \frac{\Delta L}{L \cdot \Delta T} \tag{A2}$$

$\Delta L$is the average displacement on the top edge of the representative element, L is the original length of the left and right edges and ΔT is the temperature rise of the whole representative element at the steady state.

Similarly to the tensile test, stress concentration existed in the representative element (Figure A3) when heated, which comes from the CTE mismatch between the reinforcement and the matrix.

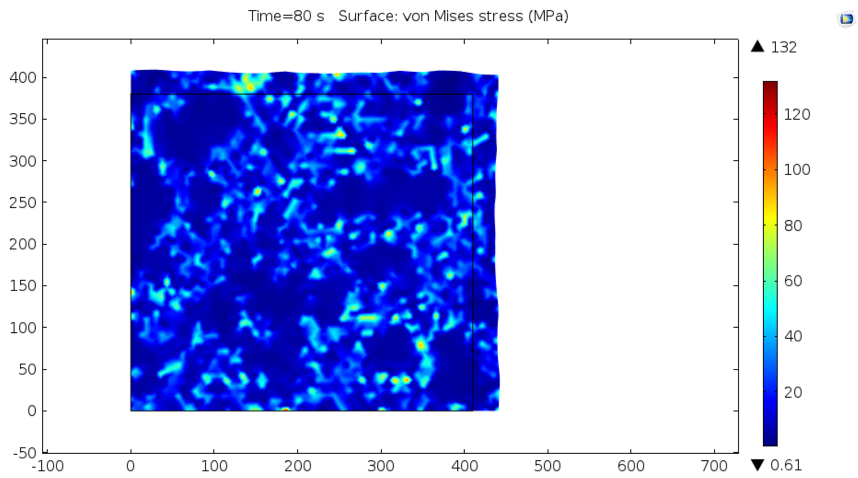

Figure A3. Stress concentration in the representative element at 80 s in virtual heat experiment.

Appendix B. Fitting the ANALYTICAL COF Function on Sliding Speed and Surface Temperature

The analytical function determined in Section 4.3 has the form given by Equation (A3) as follows

$$\mu(v,T) = c_0 + c_1 v + c_2 T + c_3 vT + c_4 T^2 + c_5 (T-300)^2 sign(T-300) \qquad \text{(A3)}$$

where c_0 through c_5 are fitting coefficients and listed in Table A1. The fitting is conducted in numerical software package MATLAB v8.6.0 (R2015b) using the Curve Fitting Toolbox [18]. The adjusted R-square of the fitting is 0.9455, suggesting a high fidelity in the analytical function in approximating the measured data from dyno tests.

Table A1. Fitting parameters and their 95% confidence bounds.

Coefficient	Fitted Value	Lower Bound	Upper Bound
c_0	−1.34	−1.44	−1.25
c_1	-3.09×10^{-3}	-3.47×10^{-3}	-2.70×10^{-3}
c_2	1.24×10^{-2}	1.18×10^{-2}	1.30×10^{-2}
c_3	5.36×10^{-6}	3.93×10^{-6}	6.79×10^{-6}
c_4	-2.21×10^{-5}	-2.30×10^{-5}	-2.12×10^{-5}
c_5	-1.97×10^{-5}	-2.08×10^{-5}	-1.86×10^{-5}

Another important feature evident from Equation (A3) is the use of sign function on a cutoff value of temperature at 300 °C. It is found in the fitting process that without this “inflection”, a fitting R-square value above 0.6 can never be achieved, strongly suggesting the inherent nature of the reverse of temperature dependence of the COF function in the investigated temperature range.

References

1 Gegel GA, Weiss DJ. Enabling Technology for the Design of Short-Fiber Reinforced Aluminum MMC Components. *International Journal of Metalcasting* 2007; **1**: 57. https://doi.org/10.1007/BF03355418.

2 Rawa SPL. Metal-Matrix Composites for Space Applications. *JOM* 2001; **53**: 14. https://doi.org/10.1007/s11837-001-0139-z.

3 Mackin TJ, Noe SC, Ball KJ, *et al*. Thermal Cracking in Disc brakes. *Engineering Failure Analysis* 2002; **9**: 63–76.

4 Talati F, Jalalifar S. Analysis of Heat Conduction in a Disk Brake System. *Heat and Mass Transfer* 2009; **45**: 1047–1059. https://doi.org/10.1007/s00231-009-0476-y.

5 Yevtushenko AA, Grzes P. Axisymmetric FEA of Temperature in a Pad/Disc Brake System at Temperature-

Dependent Coefficients of Friction and Wear. *International Communications in Heat and Mass Transfer* 2012; **39**: 1045–1053.

6 Yevtushenko AA, Adamowicz A, Grzes P. Three-Dimensional FE Model for the Calculation of Temperature of a Disc Brake at Temperature-Dependent Coefficients of Friction. *International Communications in Heat and Mass Transfer* 2013; **42**: 18–24.

7 Yevtushenko AA, Grzes P. 3D FE Model of Frictional Heating and Wear with a Mutual Influence of the Sliding Velocity and Temperature in a Disc Brake. *International Communications in Heat and Mass Transfer* 2015; **62**: 37–44.

8 Shorowordi KM, Haseeb ASMA, Celis JP. Velocity Effects on the Wear, Friction and Tribochemistry of Aluminum MMC Sliding against Phenolic Brake Pad. *Wear* 2004; **256**: 1176–1181.

9 Daoud A, Abou El-khair MT. Wear and Friction Behavior of Sand Cast Brake Rotor Made of A359-20vol% SiC Particle Composites Sliding against Automobile Friction Material. *Tribology International* 2010; **43**: 544–553.

10 Muratoğlu M, Aksoy M. The Effects of Temperature on Wear Behaviours of Al–Cu Alloy and Al–Cu/SiC Composite. *Materials Science and Engineering: A* 2000; **282**: 91–99.

11 El Sebaie O, Samuel AM, Samuel FH, *et al*. The Effects of Mischmetal, Cooling Rate and Heat Treatment on the Eutectic Si Particle Characteristics of A319. 1, A356. 2 and A413. 1 Al–Si Casting Alloys. *Materials Science and Engineering: A* 2008; **480**: 342–355.

12 Jang H, Ko KH, Kim SJ, *et al*. The Effect of Metal Fibers on the Friction Performance of Automotive Brake Friction Materials. *Wear* 2004; **256**: 406–414.

13 Newcomb TP. Temperatures Reached in Disc Brakes. *Journal of Mechanical Engineering Science* 1960; **2**: 167–177. https://doi.org/10.1243/JMES_JOUR_1960_002_026_02.

14 *COMSOL Multiphysics 4.3 User' s Guide*; COMSOL Inc.: Burlington, MA, USA, 2012; p. 22

15 Zhang H, Loukus A, Loukus J. Application of Functional Gradient Al Metal Matrix Composite as a Brake Rotor-Finite Element Analysis. *International Journal of Materials Engineering and Technology* 2010; **3**: 143–153.

16 Bassani R, Levita G, Meozzi M, *et al.* Friction and Wear of Epoxy Resin on Inox Steel: Remarks on the Influence of Velocity, Load and Induced Thermal State. *Wear* 2001; **247**: 125–132.

17 Zhang Y, NeedlemanA. On the Identification of Power-Law Creep Parameters from Conical Indentation. *Proceedings of the Royal Society A: Mathematical, Physical and Engineering Sciences* 2021; **477**(**2252**): 20210233.

18 MathWorks. *Curve Fitting Toolbox: For Use with MATLAB®: User' s Guide*; MathWorks: Natick, MA, USA, 2002.